
Aerodynamic study of a 'humpy' propeller

B.G. Marinus* and W. Bosschaerts

Department of Mechanical Engineering,
Royal Military Academy,
B-1000 Brussels, Belgium
Fax: +32-2-742-6547
E-mail: benoit.marinus@rma.ac.be
E-mail: walter.bosschaerts@rma.ac.be
*Corresponding author

M. Roger

Fluid Mechanics and Acoustics Laboratory,
Ecole Centrale de Lyon,
F-69134 Ecully, France
Fax: +33-47-218-9143
E-mail: michel.roger@ec-lyon.fr

Abstract: A detailed aerodynamic study of a 'humpy' high-speed propeller is presented. This propeller is the result of a bi-disciplinary optimisation procedure and features blade segments of wider chord bordered by narrow segments. The aerodynamic consequences of these regions are investigated and correlated to the aeroacoustic properties by comparison to an equivalent blade without hump.

Keywords: propeller; aerodynamics; aeroacoustics; chord.

Reference to this paper should be made as follows: Marinus, B.G., Bosschaerts, W. and Roger, M. (2012) 'Aerodynamic study of a 'humpy' propeller', *Int. J. Engineering Systems Modelling and Simulation*, Vol. 4, Nos. 1/2, pp.27–35.

Biographical notes: B.G. Marinus received his MSc from the Royal Military Academy, Brussels, Belgium. He is a Captain in active duty. His areas of interest concern multidisciplinary optimisation of propellers and propeller flow in general.

W. Bosschaerts is presently a Professor at the Royal Military Academy, Brussels, Belgium. He received his PhD from the University of Ghent, Belgium. His areas of interest cover general aerodynamics, heat exchange and HVAC problems.

M. Roger is a Professor at the Ecole Centrale de Lyon, Lyon, France. He received his PhD from the University of Lyon 1. His areas of interest concern the aeroacoustics of turbo machinery and rotating bodies.

This paper is a revised and expanded version of a paper entitled 'Aerodynamic study of a 'humpy' propeller' presented at the 46th Applied Aerodynamics Symposium of the French Aeronautics and Astronautics Society, Orléans, 28th–29th March 2011.

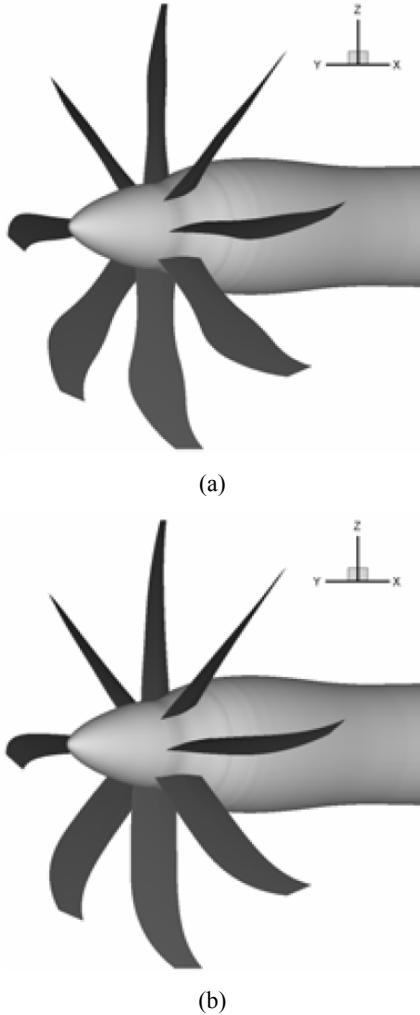
1 Introduction

Aeroacoustic and aerodynamic optimisation of high-speed propeller blades using multi-objective differential evolution with innovative optimisation parameters (Marinus et al., 2010) led to drastically new shapes exhibiting a large 'hump' [see Figure 1(a)]. It consists of a region of wide chord bordered by regions of smaller chord in disregard of the potential geometrical sweep. This is a radical departure from the advanced blade shapes that were proposed in similar efforts for high-speed propellers (Groeneweg and Bober, 1988; Gardarein and Bousquet, 2000). Humpy

blades outperformed all other shapes with respect to the objectives to be minimised. They were formulated as a weighted sum of power at different operating points for the first objective, and a weighted sum of sound pressure levels (SPL) at different locations and under different operating conditions for the second. The hump is a true result of the optimisation process and not merely an artefact of the parameterisation technique as confirmed by the large amount of blade designs analysed during the optimisation process, including 'straight' ones with or without sweep. Somehow, 'humpy' designs have an advantage that is also effective at off-design conditions. Similar results were

obtained with another optimisation, including aeroelasticity this time (Marinus et al., 2011a, 2011b). In order to investigate the effect of the hump on blade performances from an aerodynamic as well as aeroacoustic point of view, a blade is designed with the same radial distribution of sweep, twist and thickness albeit it does not feature a hump [see Figure 1(b)]. Both blades have the same activity factor (AF) and are compared.

Figure 1 ‘Humpy’ and straight propellers, (a) Propeller *A* – ‘humpy’ shape (b) Propeller *B* – straight shape



2 Blade geometry and operating conditions

The radial distributions of the parameters determining the blade shape are given in Figure 2 for both blades. In this figure, D is the propeller diameter, R its tip radius, b the chord, t the thickness, Sw the geometrical sweep, Tw the twist and r refers to the running radius. Propeller *A* features high tip sweep as visible from Figure 2(b) and a distinct chord hump centred around 65% span [see Figure 2(a)]. This blade is rather thin and has strong twist. Propeller *B* has identical distributions except for the chord that features no hump. The resulting planforms are given in Figure 3. The AF defined by

$$AF = \frac{10^5}{D^4} \int_{r_{hub}}^R \frac{b}{D} r^3 dr \tag{1}$$

is quasi identical for both propellers ($AF_A = 138.6$ and $AF_B = 138.2$). Additionally, the blades are built with the same airfoils; these are also a result of the optimisation process and are shown in Figure 4. The eight-bladed propellers have a diameter of 4.5 m and the blades have a fixed blade angle at 75%-radius β_{ref} of 63° in cruise.

Figure 2 Radial distributions defining the blade planform, (a) chord (b/D) and thickness (t/b) distributions (b) geometrical sweep (Sw) and twist (Tw) distributions

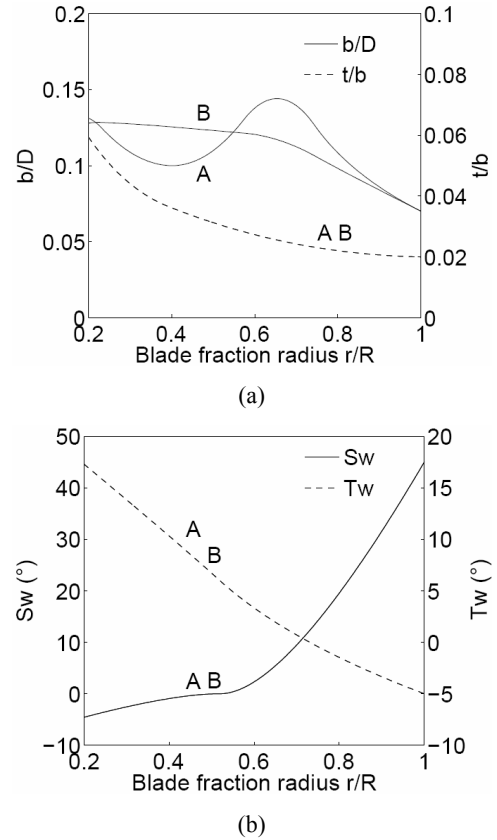


Figure 3 Blade planforms, (a) Blade *A* (b) Blade *B*

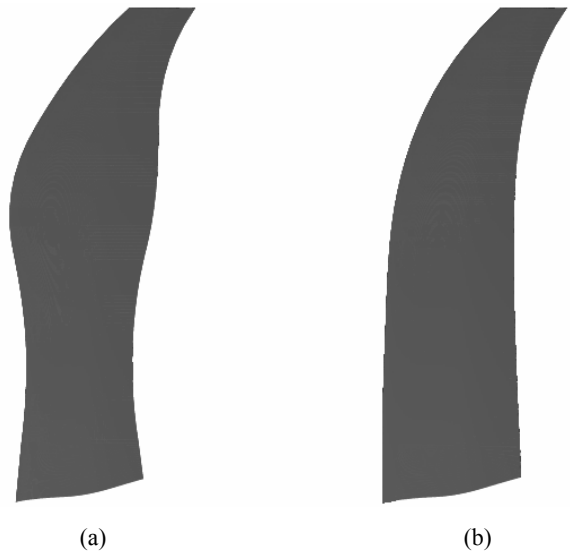
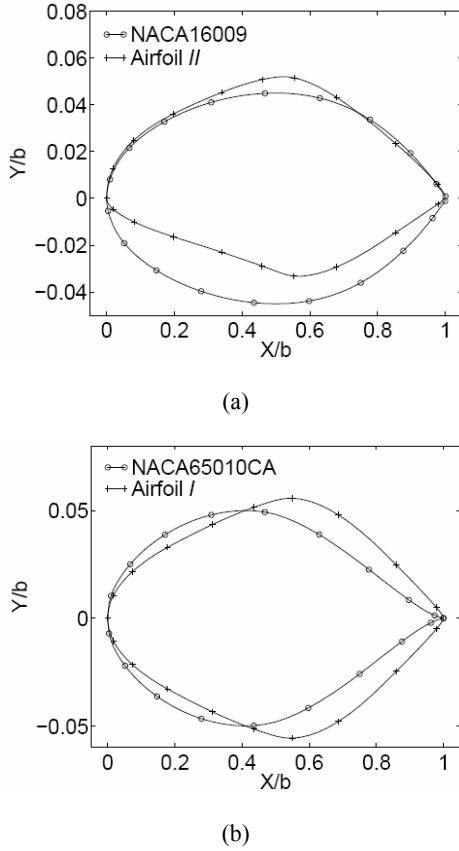


Figure 4 Airfoil geometries (Airfoil I is used from the blade root to 35% radius and Airfoil II from 45% radius to the tip), (a) Airfoil II (b) Airfoil I



The external operating conditions are summarised in Table 1 where the free-stream density of air (ρ_∞), its temperature (T_∞) and the Mach number (M_∞) are given along with the Reynolds number based on the chord at 75%-radius ($Re_{b,75\%}$). In cruise condition three advance ratios $J_{CR,i}$ are assessed; these are defined as

$$J_{CR,i} = \frac{v_\infty}{n_i D} \quad (2)$$

where v_∞ is the free-stream velocity and n_i the rotational velocity expressed in *rps* for the i^{th} operating point. For each propeller individually, $J_{CR,2}$ is adapted in order to match a cruise thrust $T_{CR,2}$ of 11 kN. Table 2 gives the resulting conditions at the design point with $P_{CR,2}$ the required power and M_{tip} the helical tip Mach number. $J_{CR,1}$ is 0.5 lower than $J_{CR,2}$ whereas $J_{CR,3}$ is 0.3 higher.

Table 1 Operating conditions at cruise

Propeller	A	B
ISA altitude (m)	10,665	
ρ_∞	0.380	
T_∞	218.81	
M_∞	0.75	
$Re_{b,75\%}$	3.75e06	3.02e06

Table 2 Design conditions

Propeller	A	B
$J_{CR,2}$	3.57	3.54
$T_{CR,2}$ (kN)	10.96	11.20
$P_{CR,2}$ (kW)	3,380	3,535
M_{tip}	0.99	1.00

Figure 5 Interblade channel

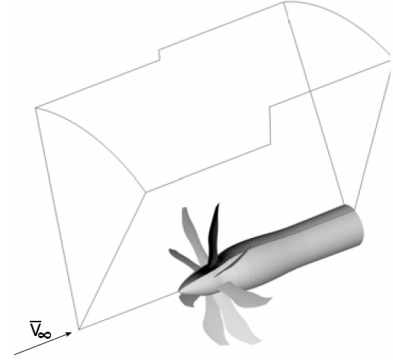
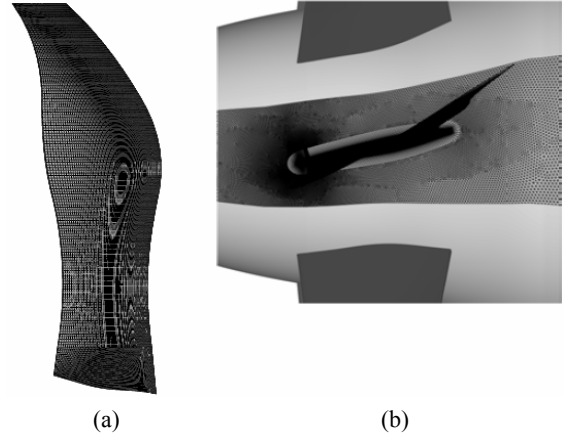


Figure 6 Surface mesh, (a) blade surface mesh (b) spinner surface mesh and O-type boundary layer mesh



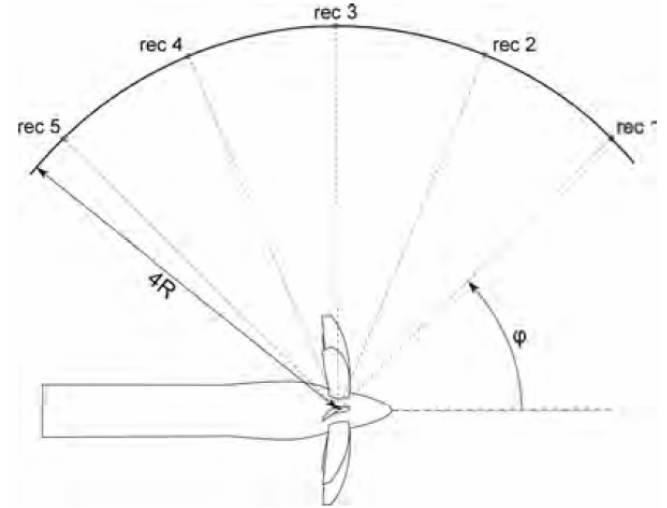
3 Computational method

Aerodynamic computations rely on the commercial code Fluent¹ to perform steady RANS simulations of a single blade passage in free air under zero angle of attack as shown in Figure 5. The governing equations are discretised using a second order central differencing scheme in space coupled to an implicit time discretisation. The full propeller is modelled using periodic boundary conditions with continuity of pressure and temperature between two adjacent blade passages. The $k - \epsilon$ realisable turbulence model (Shih et al., 1995) is used in combination with wall treatment. Adiabatic no-slip wall conditions are used for the spinner and blade surfaces whereas the test-section radial boundary is reproducing the effects of a pressure far-field. This approach has proven its robustness and accuracy as satisfactory agreement with experimental results has been found for different operating conditions over a wide range

of blade shapes (Marinus, 2007). The surface mesh of the blade is made of quadrilateral elements as shown in Figure 6(a). This mesh is extruded into an O-type boundary layer mesh [see Figure 6(b)] such that the average y^+ value on the blade surface amounts 35, which is a value consistent with the chosen turbulence model. The spinner surface mesh consists of triangles which are the basis for the tetrahedral blade passage mesh.

In the post-processing of the aerodynamic results, the sound pressure level ($SPL = 20 \log p'/2e - 5$ Pa with p' the acoustic pressure) is computed at various receiver locations for the tonal noise signal emitted by the propeller. Receivers are located at different angles ($\varphi = 45^\circ, 67.5^\circ, 90^\circ, 112.5^\circ,$ and 135°) at a distance of 4-tip radii from the axis as shown in Figure 7. To compute the SPL, the inhomogeneous wave equation derived from Lighthill's acoustic analogy by Ffowcs Williams-Hawkings (FW-H) is chosen as the theoretical background because it benefits from the partial decoupling of the acoustic and aerodynamic aspects. Solving the FW-H equation with the use of free-space Green's function and standard derivation, one obtains formulation 1A from Farassat (2007) (Farassat and Succi, 1983) expressed in a medium-fixed coordinate system (Frota et al., 1998) (i.e., the observer is assumed to translate forward at the same speed as the propeller). Equations are obtained for the thickness and loading noise, which are the dominant sources, whereas the quadrupole source term, accounting for non-linearities such as shocks or turbulence, has been dropped from the FW-H equation (Marinus et al., 2009) because of the prohibitive numerical cost of the volume integration it requires. The blade surface is chosen as integration surface for the other source terms. The validity of formulation 1A is extended in the sonic domain by the use of the truncated formulation proposed in Marinus et al. (2009).

Figure 7 Location and nomenclature of acoustic receivers



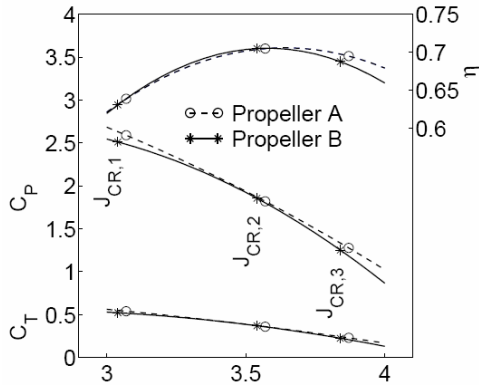
The accuracy of the results is analysed according to Celik et al. (2008). The cell size parameter h is computed from

$$h = \left[\frac{1}{N} \sum_{i=1}^N \Delta V_i \right]^{1/3} \quad (3)$$

with N the total numbers of cells and ΔV_i the volume of the i^{th} cell. The reporting quantities [grid convergence index (GCI) approximate relative error e_a and extrapolated relative error e_{ext}] are computed for C_T , C_P and SPL_{rec3} at the design cruise condition and given in Table 3. This table clearly indicates the independence of the various results with respect to mesh parameters especially for the regular and fine meshes. Note that all results shown in this paper are obtained with the fine mesh calculations.

Table 3 Grid independence results at $J_{CR,2}$

	Propeller A			Propeller B		
	Coarse mesh	Regular mesh	Fine mesh	Coarse mesh	Regular mesh	Fine mesh
Number of cells N	9.62e05	1.25e06	3.70e06	9.88e05	1.33e06	3.6706
h	0.0125	0.0115	0.0080	0.0124	0.0113	0.0080
C_T	0.3552	0.3627	0.3632	0.3605	0.3661	0.3694
C_P	1.8212	1.8378	1.8391	1.8356	1.8512	1.8548
SPL_{rec3}	111.46	112.60	112.53	113.52	114.58	114.66
C_T	GCI (%)	5.22	0.26	1.17	0.03	
	e_a (%)	2.03	0.97	1.52	0.90	
	e_{ext} (%)	4.01	0.21	0.93	0.02	
C_P	GCI (%)	0.09	0.00	0.24	0.00	
	e_a (%)	0.90	0.07	0.84	0.19	
	e_{ext} (%)	0.00	0.07	0.19	0.00	
SPL_{rec3}	GCI (%)	0.08	0.00	0.00	0.08	
	e_a (%)	1.01	0.06	0.93	0.07	
	e_{ext} (%)	0.07	0.00	0.07	0.00	

Figure 8 Aerodynamic performance curves


4 Aerodynamic comparison

Prior to the detailed analysis of the flow field, it is shown that both propellers operate in highly similar conditions (given in Table 2) even if $J_{CR,2}$ has been adjusted to match the net thrust constraint. Propeller A operates at a cruise advance ratio of 3.57 against 3.54 for Propeller B (thus a slightly higher RPM than Propeller A). Henceforth, at the design cruise condition ($J_{CR,2}$), Propeller B delivers a net thrust within 2.2% of that of Propeller A for a difference in power of the order of 4.6%. Their respective aerodynamic

performance is summarised in Figure 8 where the thrust coefficient (C_T), power coefficient (C_P) and net efficiency (η) are respectively defined as:

$$C_T = \frac{T}{\rho_\infty n^2 D^4} \quad (4)$$

$$C_P = \frac{P}{\rho_\infty n^3 D^5} \quad (5)$$

$$\eta = \frac{T v_\infty}{P} = \frac{J C_T}{C_P} \quad (6)$$

Despite differences at $J_{CR,1}$ and $J_{CR,3}$, it appears that the performance of the two propellers in terms of thrust coefficient, power coefficient and net efficiency at the design cruise condition $J_{CR,2}$ are akin, with a slight advantage in terms of power coefficient for Propeller A, as was also apparent from Table 2.

For this condition, the pressure coefficient (C_p) contours (Figure 9) indicate major differences at most radii. The pressure coefficient is defined as:

$$C_P = \frac{2}{\gamma M_\infty^2} \left(\frac{P}{P_\infty} - 1 \right) \quad (7)$$

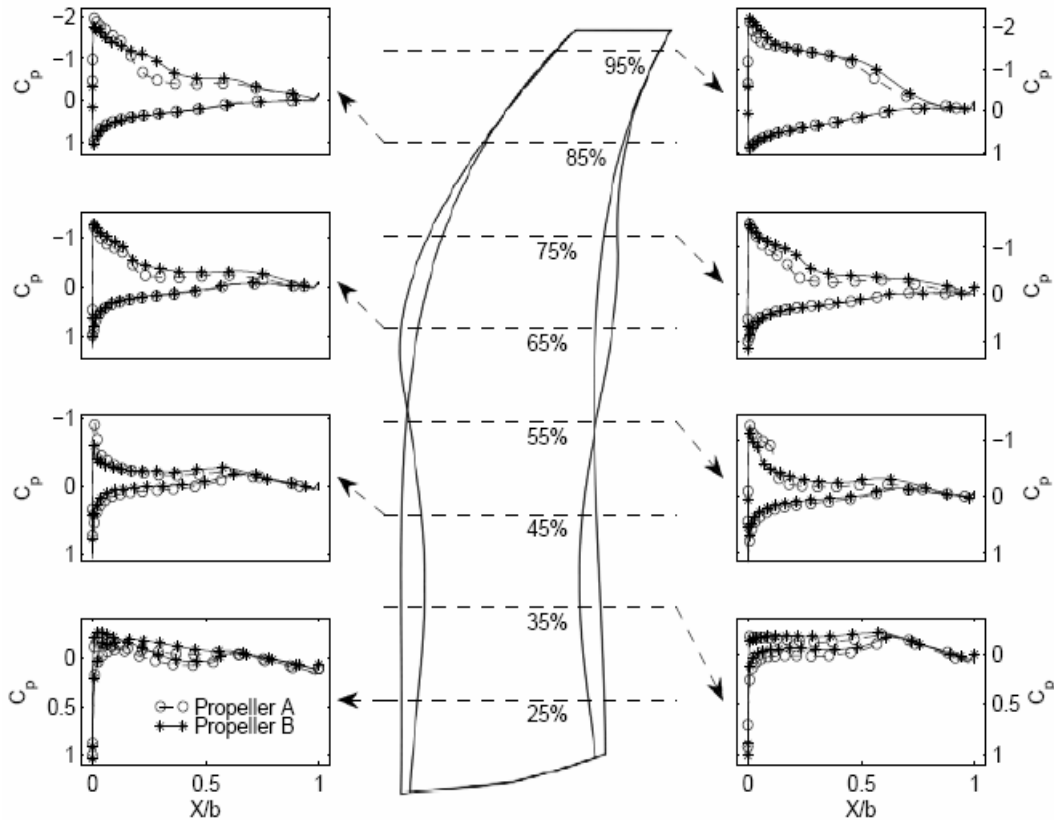
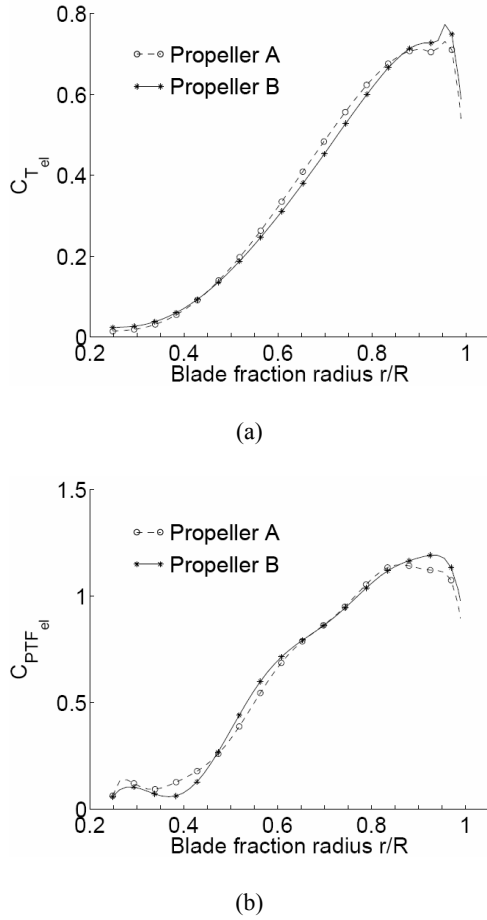
Figure 9 Pressure coefficient contours at various span (design cruise condition $J_{CR,2}$)


Figure 10 Spanwise elemental force distributions at the design cruise condition $J_{CR,2}$, (a) thrust (b) propeller torque force



These differences explain the disparities in the production of thrust and propeller torque force that appear on Figure 10 where the elemental force coefficients $C_{T_{el}}$ and $C_{PTF_{el}}$ are defined as:

$$C_{T_{el}} = \frac{T_{el}}{1/ \rho_{\infty} v_{\infty}^2 b_{mean}} \quad (8)$$

$$C_{PTF_{el}} = \frac{PTF_{el}}{1/ \rho_{\infty} v_{\infty}^2 b_{mean}} \quad (9)$$

and have been non-dimensionalised by the mean chord $b_{mean} = (1/S) \int b(r) dr$ (with S the blade planform area) in order to establish a proper base for comparisons between the two blades. As indicated on Figure 9, one should bare in mind that both propellers do not have the same local chord so that direct translation of the shape of pressure contours into potential benefits for forces should be done with some care.

At lower radius (25% and 35%), the pressure distributions have the same shape though slightly shifted toward negative C_p -values for the straight blade. These

curves confirm that, for both propellers, very little forces are generated at these stations. Analysis of the velocity triangle for these two radii reveals that the sections operate at incidence angles close to 0 hence more camber should be allowed for Airfoil *I* if one wants to retrieve forces from this part of the blade.

At 45% radius from where Airfoil *II* is used, the pressure distributions are highly similar. The low pressure peak close to the leading edge, also visible at higher radii, is the consequence of rather thin sections [see Figure 2(a)]. The low camber of the airfoils results in the absence of loading on the rear part of those. The positive C_p on the pressure side close to the leading edge indicates favourable loading of this portion. This pressure side load is present at all higher radii. The net result of the leading-edge loading for the 45% section is force generation albeit in a very feeble way as apparent from Figure 10. Despite the differences in chord, this section generates net forces that are nearly identical for the two blades.

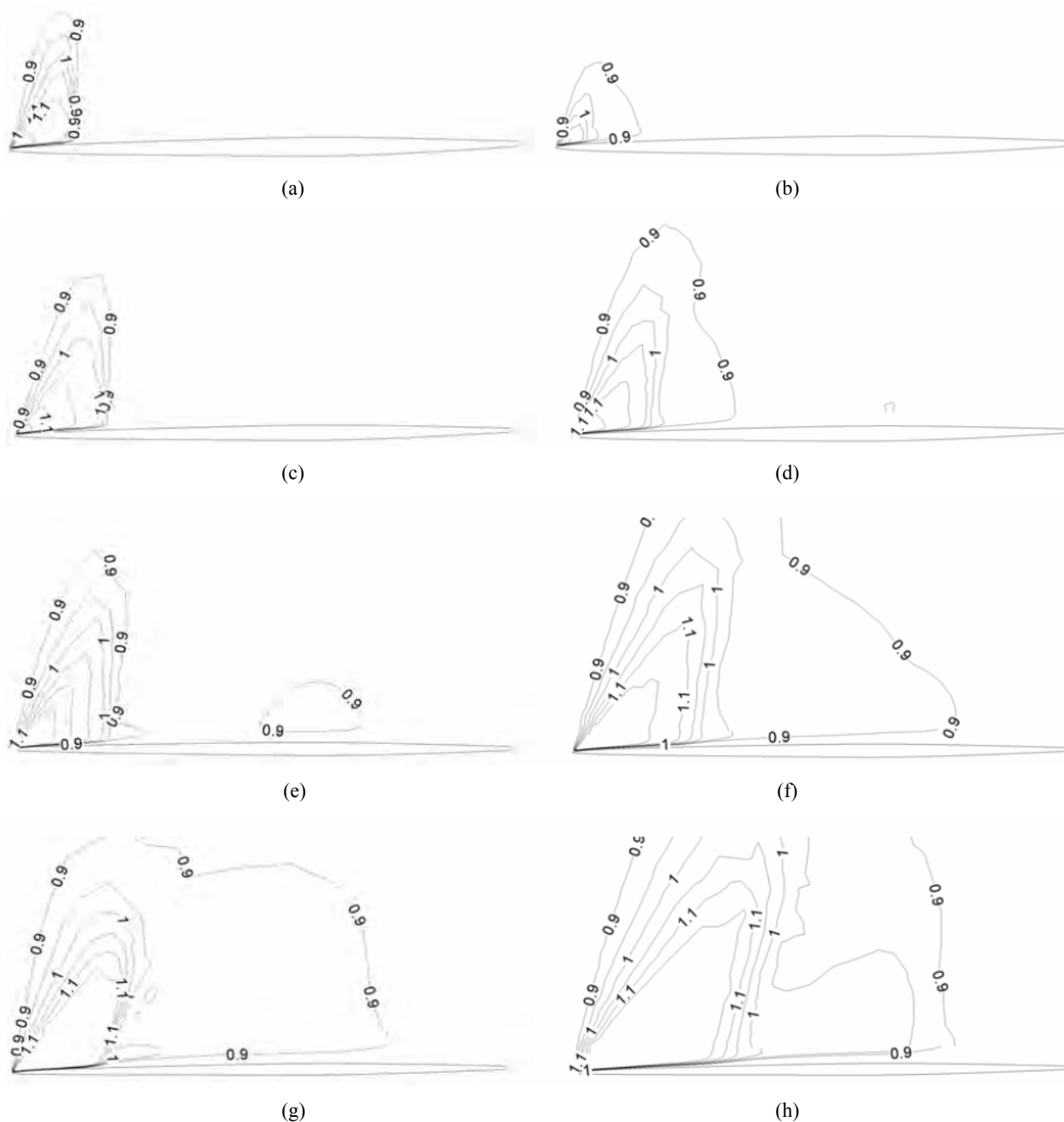
It is only at 55% radius, where both blades have the same chord that differences in thrust tend to be marked. In terms of pressure, Propeller *A* is characterised by a stronger compression due to a sharper shock [see Figure 11(a)] whereas Propeller *B* has a weaker shock [see Figure 11(b)]. Therefore, the shock on Propeller *A* does not penetrate as deep into the boundary layer as the one of Propeller *B* which degenerates into Prandtl-Meyer compression lines and penetrates more deeply. This shock is located more upstream than for Propeller *A*. In the case of Propeller *A*, the location of the shock is also the onset of separation as the skin friction coefficient is zero at this point. This is confirmed by the flat shape of the C_p -curve. Despite that, the section produces a bit more thrust for slimly lower propeller torque force.

At 65% radius, the shock is again somewhat weaker for the straight blade as is apparent from Figures 11(c) and 11(d) and results in more favourable suction. But this does not translate into more thrust as is apparent from Figure 10(a). The disadvantage due to the lame pressure distribution of the humpy blade is entirely compensated by its wider chord.

At 75% radius, Propeller *A* has more compression and a sharper shock located upstream of the shock position for Propeller *B* [see Figures 11(e) and 11(f)]. Though the pressure distribution for Propeller *A* is nearly flat downstream of the shock, no separation occurs. Here again, the wider chord offsets the somewhat low-grade pressure distribution.

At 85% radius, where most of the thrust is generated and where both chords get similar again, it is mostly the additional suction provided toward the leading edge that allows for more thrust to be produced by the humpy blade (see Figures 9 and 10). The shock is lightly stronger for Propeller *A* so it penetrates less deeply into the boundary layer. As for the previous station, the shock is located more upstream and is sharper for the humpy design [see Figures 11(g) and 11(h)].

Figure 11 Iso-Mach lines at $J_{CR,2}$. (a) Propeller A – 55%-radius (b) Propeller B – 55%-radius (c) Propeller A – 65%-radius (d) Propeller B – 65%-radius (e) Propeller A – 75%-radius (f) Propeller B – 75%-radius (g) Propeller A – 85%-radius (h) Propeller B – 85%-radius



Finally, at 95% radius, both pressure distributions and both chords are highly similar though there is a more interesting suction in the case of the straight blade. The net result is in favour of thrust but with a strong penalty in propeller torque force. For this station, a compression extending chordwise is present around 0.6.

For all transonic stations, it is interesting to notice the forward position of the shock well before the crest [see Figure 4(a)], a feature known to come with less wave drag than if the shock would be more downstream. From a purely aerodynamic point of view, both propellers deliver identical net performance with nearly the same efficiency notwithstanding the fact that the hump comes with slightly

higher shock strengths. Hence, the previous results suggest that three dimensional effects play a vital role and are effectively driven by the chord distribution. To exploit all the benefits of the humps to a bigger extent, additional trimming of the airfoil is needed in order to investigate the benefits of enhancing the shape of the pressure distribution so that part of the load is shifted to the aft part of the airfoil. Aside from these considerations, the distribution of thrust [Figure 10(a)] suggests that the increment in blade surface contributes effectively to the production of forces so that higher advance ratios yield the same overall thrust.

The previous observations are confirmed by looking at Figures 12(a) and 12(c) that show isobars on the suction

side of the blade. Below 35% radius and above 95% radius, both propeller have very similar flow conditions. At 95% radius, the compression occurs almost at constant radius and that contrasts with its otherwise spanwise extent. The blade tip operates shock-free in both cases. The most striking features in the mid-span region, are the differences in shock behaviour. From 45% radius, a shock is present on the suction side of both blades though it starts from a slightly higher radius for the straight blade. At 55% radius, the main difference lies within the location of the shock: closer to the leading-edge for the straight blade. This is purely the result of 3D effects as both blades share the same airfoil and, for this section, the same chord. From 65% to 85%, the shock strength is different as indicated by the stronger focussing of isobars for the humpy blade that is the consequence of more pronounced shocks. These differences translate into quite different behaviours in terms of vorticity. Vortical structures are visualised on Figures 12(b) and 12(d) by the λ_2 -criterion (Jeong and Hussain, 1995). In both cases, the trailing-edge vorticity is contained within one chord downstream of the blades. On the contrary, substantial differences are visible for the leading-edge vortex and the shock-induced vorticity due to baroclinic effects even in these rather weak shocks (Kevlahan, 1997). The spatial extent of the leading-edge vortex is clearly somewhat smaller at 65% radius for Propeller *A* than for Propeller *B*. On the outboard part, the hump on Propeller *A* causes both types of vorticity to merge much earlier (at 75%) than for the straight blade; this is also because the stronger shock on Propeller *A* is responsible for more vorticity due to baroclinic effects. At 85%-radius, the vortical structures of Propeller *A* have a bigger extent than those of Propeller *B*. Nevertheless, this does not have a significant effect on the extent and path of the tip vortex which is similar for both blades.

5 Aeroacoustic comparison

Concerning noise generation at the design point $J_{CR,2}$, Figure 13 gives the directivity pattern for the two propellers in the design cruise condition for the thickness and loading noise together. The quadrupole noise is not dominant for such thin and highly swept blades (Hanson and Fink, 1979; Brooks, 1980). This corresponds to a tip Mach number M_{tip} of 1.003 for Propeller *B* versus 0.999 only for Propeller *A* thanks to the extra blade surface at three quarter span. The figure shows that the humpy blade is effective in and aft of the propeller plane but radiates more sound in the upstream direction. As such, the differences in tip Mach number do not suffice to explain the difference in SPL at the propeller plane as in both cases the flow over the tip part of the blade, where sound is produced in a very effective way, is extremely similar. Hence the hump and the leading-edge taper it induces, act to decrease the sound level emitted in the propeller plane by favourable interferences (Hanson, 1980) and by shifting part of the thrust load toward 70% radius. The directivity pattern also suggests that the sound energy which is not emitted in the rotational plane and the

downstream direction is quite effectively emitted in the upstream direction.

Figure 12 Iso-contours of pressure coefficient C_p (a, c) and vortical structures visualised by surfaces of iso- λ_2 criterion (b, d) at design cruise condition $J_{CR,2}$ (a) isobars – Propeller A (b) Propeller A (c) isobars – Propeller B (d) Propeller B

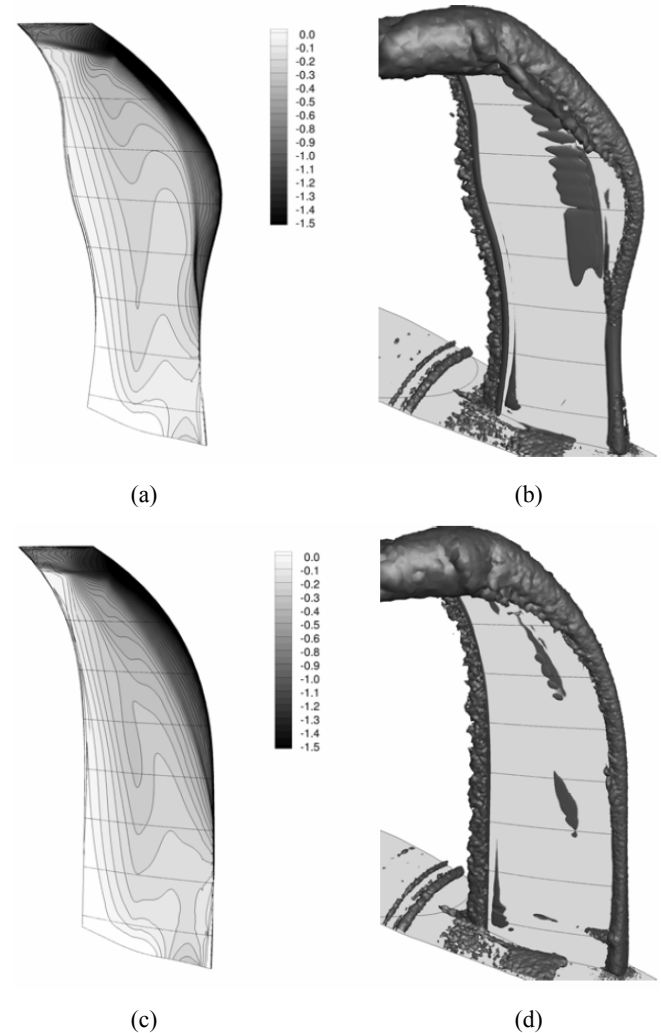
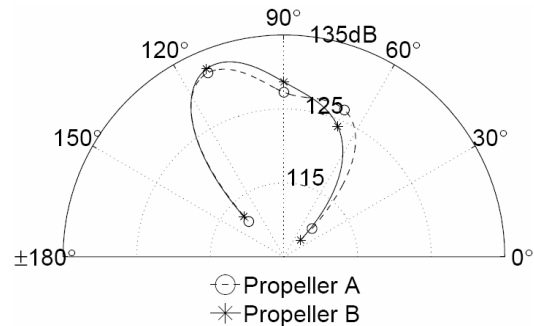


Figure 13 SPL directivity at $J_{CR,2}$



6 Conclusions

The present analysis compares a humpy and a straight blade having identical AFs as well as airfoils and operating at

constant load in given flight conditions. The results show how the three dimensional flow is strongly affected by the chord distribution in particular for shock intensity and its chordwise location. The net result is a decrease in required power for constant thrust and an increase in advance ratio. The additional surface at moderate radius, provided by the hump allows part of the load to be shifted from the tip. This helps in reducing effectively the SPL in and downstream of the propeller plane although the acoustic energy that is not radiated in those directions is radiated in the upstream one. Given the observations done at various radius, it is comforting to notice that the airfoils obtained by the optimisation process described in Marinus et al. (2010), feature interesting attributes of transonic airfoils even if there is room for potential improvements. Obviously, the obtained blade shapes have also been examined for mechanical strength issues a posteriori (Marinus, 2011).

Acknowledgements

The authors wish to acknowledge the Belgian Defence Scientific and Technologic Research initiative for its funding of the present study.

References

- Brooks, B.M. (1980) 'Acoustic measurement of three prop-fan models', *Proceedings of the 6th AIAA Aeroacoustics Conference*, AIAA, Halford, USA, June, AIAA 80-0995.
- Celik, I.B., Ghia, U., Roache, P.J., Freitas, C.J., Coleman, H. and Raad, P.E. (2008) 'Procedure for estimation and reporting of uncertainty due to discretization in CFD applications', *Journal of Fluids Engineering*, July, Vol. 130, No. 7, pp.1–4.
- Farassat, F. (2007) 'Derivation of formulations 1 and 1a of Farassat', Technical Memorandum, NASA, TM-2007-214853, NASA Langley Research Center, USA, March.
- Farassat, F. and Succi, G.P. (1983) 'The prediction of helicopter rotor discrete frequency noise', *Vertica*, Vol. 7, No. 4, pp.309–320.
- Frota, J.M., Lempereur, P. and Roger, M. (1998) 'Computation of the noise of a subsonic propeller at an angle of attack', *Proceedings of the 4th AIAA/CEAS Aeroacoustics Conference*, AIAA, Toulouse, France, June, AIAA 1998-2282.
- Gardarein, P. and Bousquet, J.M. (2000) 'ONERA propeller aerodynamic activities in Brite-Euram programmes APIAN-GEMINI', *Workshop on European Research on Aerodynamic Engine/Airframe Integration for Transport Aircraft*, Braunschweig, Germany, September.
- Groeneweg, F.F. and Bober, L.J. (1988) 'NASA Advanced propeller research', Technical memorandum, NASA, Lewis Research Center, USA, TM-101361.
- Hanson, D.B. (1980) 'Influence of propeller design parameters on far-field harmonic noise in forward flight', *AIAA Journal*, November, Vol. 18, No. 11, pp.1313–1319.
- Hanson, D.B. and Fink, M.R. (1979) 'The importance of quadrupole sources in prediction of transonic tip speed propeller noise', *Journal of Sound and Vibration*, Vol. 62, No. 1, pp.19–38.
- Jeong, J. and Hussain, F. (1995) 'On the identification of a vortex', *Journal of Fluid Mechanics*, Vol. 285, pp.69–94.
- Kevlahan, N.K.-R. (1997) 'The vorticity jump across a shock in a non-uniform flow', *Journal of Fluid Mechanics*, Vol. 341, pp.371–384.
- Marinus, B.G. (2007) 'Multidisciplinary evaluation of known propeller configurations', Project Report, von Karman Institute for Fluid Dynamics, PR 2007-15, Rhode-Saint-Genèse, Belgium, June.
- Marinus, B.G. (2011) 'Toward multidisciplinary optimization of propeller blades', *Symposium on VKI's Doctoral Candidate Research*, von Karman Institute for Fluid Dynamics, Rhode-Saint-Genèse, Belgium, February–March.
- Marinus, B.G., Roger, M. and Van den Braembussche, R.A. (2010) 'Aeroacoustic and aerodynamic optimization of aircraft propeller blades', *Proceedings of the 16th AIAA/CEAS Aeroacoustics Conference*, AIAA, Stockholm, Sweden, June, AIAA 2010-3850.
- Marinus, B.G., Roger, M., Van den Braembussche, R.A. and Bosschaerts, W. (2011a) 'Multidisciplinary optimization of propeller blades: focus on the aeroelastic results', *Proceedings of the 47th AIAA/ASME/SAE/ASEE Joint Propulsion Conference & Exhibit*, AIAA, San Diego, USA, June, AIAA 2011-6059.
- Marinus, B.G., Roger, M., Van den Braembussche, R.A. and Bosschaerts, W. (2011b) 'Multidisciplinary optimization of propeller blades: focus on the aeroacoustic results', *Proceedings of the 17th AIAA/CEAS Aeroacoustics Conference*, AIAA, Portland, USA, June, AIAA 2011-2801.
- Marinus, B.G., Roger, M., Van den Braembussche, R.A. and Bosschaerts, W. (2009) 'Truncated method for propeller noise prediction up to low supersonic helical tip Mach numbers', *Proceedings of the 15th AIAA/CEAS Aeroacoustics Conference*, AIAA, Miami, USA, May, AIAA 2009-3330.
- Shih, T.-H., Liou, W.W., Shabbir, A., Yang, Z. and Zhu, J. (1995) 'A new k- ϵ eddy-viscosity model for high Reynolds number turbulent flows – model development and validation', *Computer & Fluids*, Vol. 24, No. 3, pp.227–238.

Notes

- 1 Fluent v12.0.16.